Pomeranchuk Instability Induced by an Emergent Higher-Order Van Hove Singularity on the Distorted Kagome Surface of $Co_3Sn_2S_2$

Pranab Kumar Nag,[1,*] Rajib Batabyal,[1,*] Julian Ingham,[2,*] Noam Morali,[1,*] Hengxin Tan,[1] Jahyun Koo,[1] Jean Souza,[1] Moshe Haim,[1] Armando Consiglio,[3] Enke Liu,[4] Raquel Queiroz,[2] Ronny Thomale,[3] Binghai Yan,[1,5] Claudia Felser,[4] Nurit Avraham,[1] and Haim Beidenkopf[1,†]

[1]*Condensed Matter Physics, Weizmann Institute of Science, Rehovot, 7610001, Israel*
[2]*Department of Physics, Columbia University, New York, New York 10027, USA*
[3]*Institute for Theoretical Physics and Astrophysics, University of Würzburg, Würzburg, D-97074, Germany*
[4]*Max Planck Institute for Chemical Physics of Solids, Dresden, D-01187, Germany*
[5]*Department of Physics, The Pennsylvania State University, University Park, Pennsylvania 16802, USA*

(Received 21 January 2025; revised 10 May 2026; accepted 30 July 2026; published 15 September 2026)

Materials hosting flat bands at the vicinity of the Fermi level promote exotic symmetry broken states. Common to many of these are Van Hove singularities at saddle points of the dispersion or even higher-order Van Hove singularities (HOVHSs) where the dispersion is flattened further. The band structure of kagome metals hosts both a flat band and two regular saddle points flanking a Dirac node. We investigate the kagome ferromagnetic metal $Co_3Sn_2S_2$ using scanning tunneling spectroscopy. We identify a new mechanism by which a triangular distortion on its kagome Co_3Sn surface termination considerably flattens the saddle point dispersion and induces an isolated HOVHS with algebraically divergent density of states pinned to the Fermi energy. The distortion-induced HOVHS precipitates a Pomeranchuk instability of the Fermi surface, resulting in the formation of a series of nematic electronic states. We visualize the nematic order across an energy shell of about 100 meV in both real, reciprocal, and momentum spaces, as a cascade of wave function distributions which spontaneously break the remaining rotational symmetry of the underlying distorted kagome lattice, without generating any additional translational symmetry breaking. It signifies the spontaneous removal of a subset of saddle points from the Fermi energy to lower energies. By tracking the electronic wave function structure across the deformed Fermi surface, we further identify a charge pumpinglike evolution of the wave function center of mass. The mechanism we find for the generation of higher-order saddle points under a kagome distortion may be common to other kagome materials, and potentially other lattice structures, suggesting a generic new avenue for inducing unconventional electronic instabilities toward exotic states of matter.

DOI: 10.1103/2jst-psds

Subject Areas: Condensed Matter Physics

I. INTRODUCTION

Recent years have seen increasing ability to manipulate band structures and induce flat bands in the vicinity of the Fermi energy. Ubiquitous to many of these systems are saddle points in the dispersion which generate Van Hove singularities (VHSs) in the density of states (DOS) [1]. Near these points, the DOS is logarithmically divergent, leading to the appearance of exotic electronic states of matter with spontaneously broken symmetries. There are a few known mechanisms that further squeeze the dispersion around such saddle points via inducing adjacent gaps in the band structure. This enhances the logarithmic divergence into a higher-order VHS (HOVHS) with an algebraically divergent DOS, at which the leading momentum dependence of the dispersion is of quartic or even higher power [2–7]. The HOVHS breaks the weak coupling dominance of superconducting pairing over density wave and nematic orders, thus promoting high-temperature realizations of exotic electronic order [7–9]. A prime example is given by magic angle twisted bilayer graphene, in which hybridization of the Dirac bands from the two layers produces minibands with a significantly reduced bandwidth. As the hybridization gaps increase they progressively flatten the band, generating an HOVHS [3]. A plethora of correlated phases are found in this system at partial fillings [10,11], yet the twisted angle is not an equilibrium state of the

*These authors contributed equally to this work.
†Contact author: haim.beidenkopf@weizmann.ac.il

bilayer, resulting in twist angle disorder across the device [12]. Bernal stacking of bilayer graphene, which is an equilibrium configuration, also hosts a saddle point whose dispersion can be further flattened by application of a displacement field which gaps the adjacent Dirac nodes [13–15], and similarly in the metastable rhombohedral trilayer graphene [16,17]. All these scenarios require either nonequilibrium stacking or the application of external perturbations to generate an HOVHS and thereby induce an electronic instability.

Kagome lattices intrinsically host spectroscopic features with high DOS, as their band structure comprises both a flat band and two sets of saddle points pinned to the M high symmetry momenta at energies above and below a Dirac node pinned at K. There are several material realizations of layered kagome metals that display a variety of instabilities or correlated states [18]. When the flat band is at the vicinity of the Fermi level, heavy-fermion-like phenomenology appears to arise in Ni_3In [19] and Mn_3Sn [20], and Mott-like phenomenology as in CoSn [21]. Yet, the flatness of this band is not protected, and it can become dispersive under various perturbations, such as the presence of longer-range hoppings. In contrast, the saddle points are more robust and support a variety of spontaneously symmetry broken states, most commonly charge density waves possibly with exotic character, as in the AV_3Sb_5 family (A = K, Rb, Cs) [22–28] and in FeGe [29,30]. Signatures of nematic state unrelated to charge density wave order have been reported in $CsTi_3Bi_5$ [31] and ScV_6Sn_6 [32]. However, their origin in an intrinsic motif of the kagome band structure has remained unclear.

II. RESULTS

$Co_3Sn_2S_2$ is a member of the shandite material family and develops ferromagnetic order below 175 K. It is characterized as a time-reversal symmetry broken Weyl semimetal, with Weyl nodes residing about 105 meV above the Fermi energy [33,34]. The layered crystal structure of $Co_3Sn_2S_2$ consists of Co_3Sn layers in which the Co ions are arranged in a kagome structure [Fig. 1(a)], and are covalently bonded to triangularly coordinated S and Sn layers. STM measurements require freshly cleaved surfaces, where the common cleave planes expose either the Sn or the S termination. The kagome nature has been previously probed indirectly through the Sn or S termination layers [35]. Very rarely, however, a Co_3Sn termination is exposed, allowing direct investigation of the electronic spectroscopy in the presence of the kagome structure. The topographic images depicted in Fig. 1(b) demonstrate such a termination where a flat Co_3Sn terrace appears among a dense sequence of rough crystallographic step edges cleaved along a plane about 3.5° above the (001). Higher resolution imaging [Fig. 1(c)] reveals a hexagonal pattern characteristic of kagome surfaces. Our identification of the distinct surface terminations [36], and particularly that of Co_3Sn, relies on a combination of topography, spectroscopy, quasiparticle interference (QPI), defect structures, and step edges among surfaces [33]. It agrees with more recent identifications based on STM [41] as well as atomic force microscopy [42]. Finer resolution topography [Fig. 1(d)] further finds that the C_6 symmetry of the kagome Co_3Sn layer is broken on the surface down to C_3 as three out of the six corner-sharing triangular sites around the hexagon appear slightly elevated relative to the other three, as was also imaged by others [43]. Such a surface reconstruction is rather natural due to the explicit inversion symmetry breaking introduced by cleaving. Indeed, *ab initio* calculations find that the Co_3Sn surface strongly reconstructs by an inward shift of the Co ions by about 10% of the initial Co–Co bond length away from the S ions, a layer below [Fig. 1(e)].

In differential conductance (dI/dV) spectroscopy, we find a signature for the existence of a singular DOS at the Fermi level in the form of a robust zero-bias peak [Fig. 1(f)]. It is unique to the Co_3Sn termination of $Co_3Sn_2S_2$ (see spectroscopies of Sn and S [36]). The sharp rise of the DOS on negative energies is better captured by a power law characteristic of an HOVHS than a logarithm that signifies regular VHS [Fig. 1(f) inset, pink and blue lines, respectively]. Once we allow both the exponent and a constant offset dI/dV to be free-fitting parameters, which may originate from either surface or bulk contributions, the best fit yields a power of $-1/4$. This is in agreement with an HOVHS with a quartic first nonvanishing expansion coefficient for the dispersion. Excluding such background, the fit finds a stronger divergence characterized by a power of $-1/2$ [36], suggesting the zero-bias divergence is of at least power $-1/4$. Intriguingly, on the Sn termination of $Co_3Sn_2S_2$, we find quasiparticle interference patterns that seem to correspond to an HOVHS in the vicinity of the Fermi energy [36].

In the *ab initio* surface-projected band structure [Fig. 1(g)], we find a single isolated surface band with a saddle point which crosses the Fermi level at the M point [36]. The dispersion turns from holelike along the M–Γ direction to electronlike along M–K (blue and red segments, respectively), reminiscent of the saddle point of a kagome layer. Since it has no trace in the bulk band structure [36], we conclude that it results from a two-dimensional surface state bound at the Co_3Sn termination, which exhibits the kagome potential. It does not disperse through the Weyl node [36] so it is not a Fermi-arc state but a trivial surface band that forms on the Co_3Sn termination. The hole side of the dispersion along M–Γ is extremely flat, decreasing only by about $W \approx 20$ meV across a third of the Brillouin zone, on the same order as canonical flat band systems [44–46], especially considering the strong interactions U they were shown to exhibit [47], yielding $U/W > 100$. We fit the dispersion along the M–Γ and M–K directions with a polynomial [Fig. 1(h) [36]]. While the electronlike dispersion is fairly quadratic, the holelike dispersion along M–Γ has a null quadratic coefficient, a finite

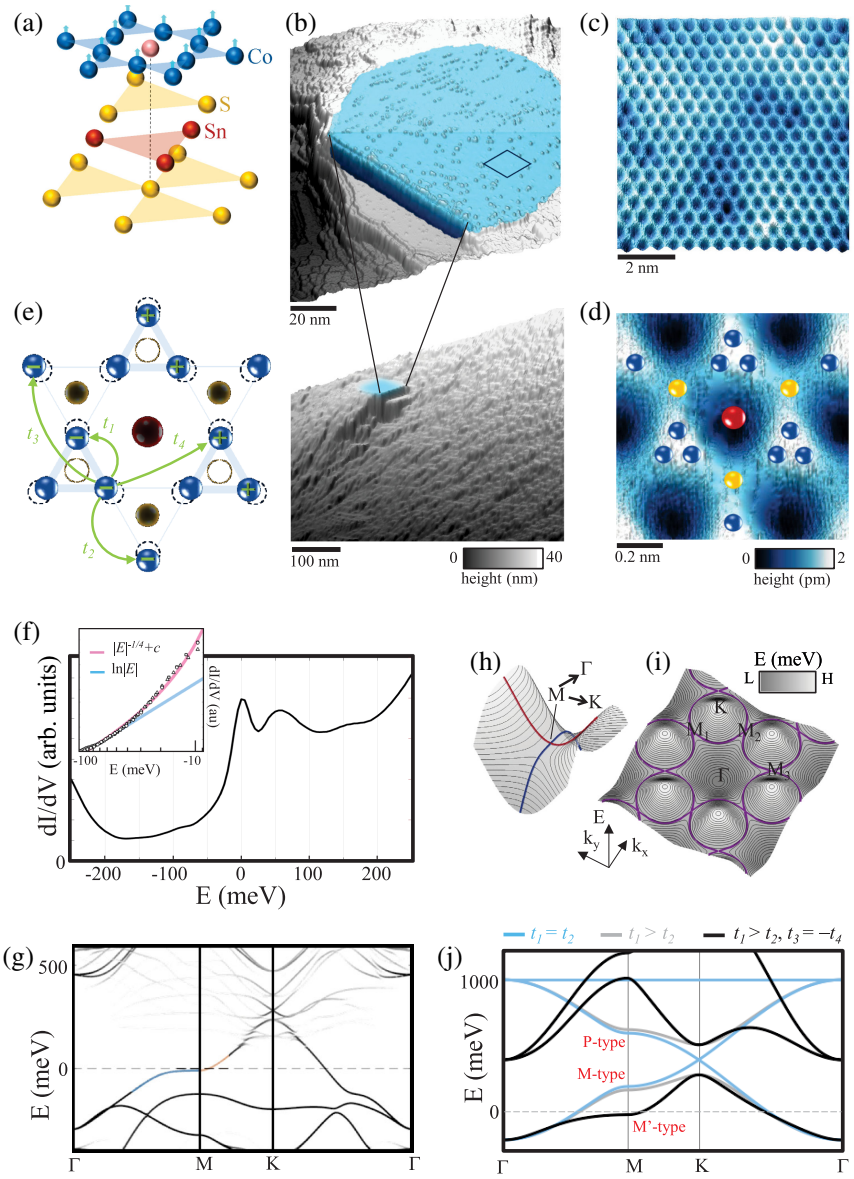

FIG. 1. Higher-order Van Hove singularity in a distorted kagome lattice. (a) The crystal structure of $Co_3Sn_2S_2$ with kagome Co arrangement. (b) Topographic images of the Co_3Sn terrace. (c) Enlarged topography. (d) Highest resolution topography shows triangular reconstruction. (e) The reconstruction away from the underlying S ions that explicitly break the symmetry. (f) dI/dV spectrum showing a zero-bias peak. The inset enlarges the negative bias side of the zero-bias peak (circles correspond to the same dataset, squares and triangles are taken from two other datasets) with best fits to a logarithm, $\ln|E|$ (blue linear line in semi-log plot), and to a power law with constant offset yielding a power of $-1/4$ (pink line). (g) DFT calculation of $Co_3Sn_2S_2$ band structure projected to the Co_3Sn surface, relaxed by triangular reconstruction. The blue and red segments correspond to the holelike and electronlike dispersions around M, respectively. (h) Flat saddle point extracted from DFT and fitted with quadratic and quartic polynomials (red and blue lines, respectively). (i) Valence band of a distorted kagome lattice with HOVHS at the equienergy contour denoted by a purple line. (j) Tight-binding band structure of an unperturbed kagome lattice, kagome with lowest order triangular distortion ($t_1 > t_2$), and kagome also with opposite sign interunit cell hopping ($t_3 = -t_4$) shown in blue, grey and black, respectively.

quartic coefficient, and requires a dominant sixth-power coefficient to accurately capture the flattened dispersion. This formally endows the saddle point as an HOVHS, where the Jacobian and Hessian of the dispersion vanish.

We trace the generation of the HOVHS to the surface reconstruction. We compare the surface-projected *ab initio* slab calculations with and without the Co reconstruction [36]. The most prominent change is a downward shift in the saddle point energy by about 100 meV. Since the bands at the Γ and K points are hardly affected, it results in a pronounced flattening of the holelike dispersion along Γ–M that generates the HOVHS, without any apparent

fine-tuning. The Fermi surface develops a pointed, snowflake shape, near which the DOS diverges as a power law [36], both characteristic of an HOVHS. The chemical potential becomes pinned to the saddle point due to its large DOS.

This, therefore, marks a novel mechanism for generating an HOVHS in kagome metals. We demonstrate its generality by reproducing it in a minimal tight-binding model of a distorted kagome lattice. We position the d_{z^2} orbitals of the Co atoms, which contribute the most to the orbital weight at the saddle point [36], on a distorted kagome lattice. We consider hopping terms t_i up to the fourth nearest neighbor, $i = 1$–4 [arrows in Fig. 1(e)]. Setting $t_1 = t_2$ and $t_3 = t_4 = 0$ reproduces the undistorted kagome band structure [Fig. 1(j), blue lines]. We first break the symmetry between nearest neighbor hopping on the distorted triangles by setting $t_1 > t_2$ while $t_3 = t_4 = 0$. The main outcome of such distortion [Fig. 1(j), gray lines] is the gapping of the Dirac node at the K point due to broken C_2 symmetry. We next include symmetry breaking in the higher-order hopping terms by setting $t_3 = -t_4$. Consequently, the m-type saddle point shifts downward in energy while the bands at the Γ and K points are unaffected. We confirm that this results in a considerable flattening of the hole dispersion of the saddle point, generating an HOVHS. Fitting the functional dependence of the DOS in the vicinity of the VHS yields algebraic energy dependence with a power of -0.25 [36] signifying an HOVHS.

The distorted tight-binding dispersion captures well the *ab initio* surface band structure [36]. We find the analytic dependence of the saddle point dispersion in the tight-binding model, $\epsilon(\mathbf{k}) = a_x k_x^2 - a_y k_y^2 + b_x k_x^4 - b_y k_y^4 + b_{xy} k_x^2 k_y^2 + \cdots$, on the hopping coefficients, $t_1 \ldots, t_4$ [36]. The coefficients that make the prefactor of the quadratic hole term vanish, $a_y(t_1 \ldots, t_4) = 0$, are consistent with the polynomial fitting of the density functional theory (DFT). We note that $t_{3,4}$ do not have to be exactly equal in magnitude for the quadratic coefficient of the dispersion to vanish [36]. The generation of an HOVHS under such a perturbation is unique to the m-type saddle point, and does not develop for the p-type VHS. Consistently, the m-type nature may enforce the relative π phase of the higher-order hopping terms as the M point position at the edge of the Brillouin zone implies a relative sign flip among those rows of contributing sites, marked in Fig. 1(e).

Next, we show that in the presence of the HOVHS at the Fermi energy, the surface electrons on the distorted Co_3Sn surface exhibit a spontaneous symmetry breaking. We image spectroscopically the spatial distribution of the local DOS across the Co_3Sn termination in a region free from any topographically visible surface impurities [Fig. 2(a)]. We then image the spatial modulation of the differential conductance over that surface with subatomic resolution across the bias interval of -250 to 250 meV [Fig. 2(b) [36]]. All these patterns appear similar as they have the same periodicity. Accordingly, no new Bragg peaks are detected in Fourier space. However, when we

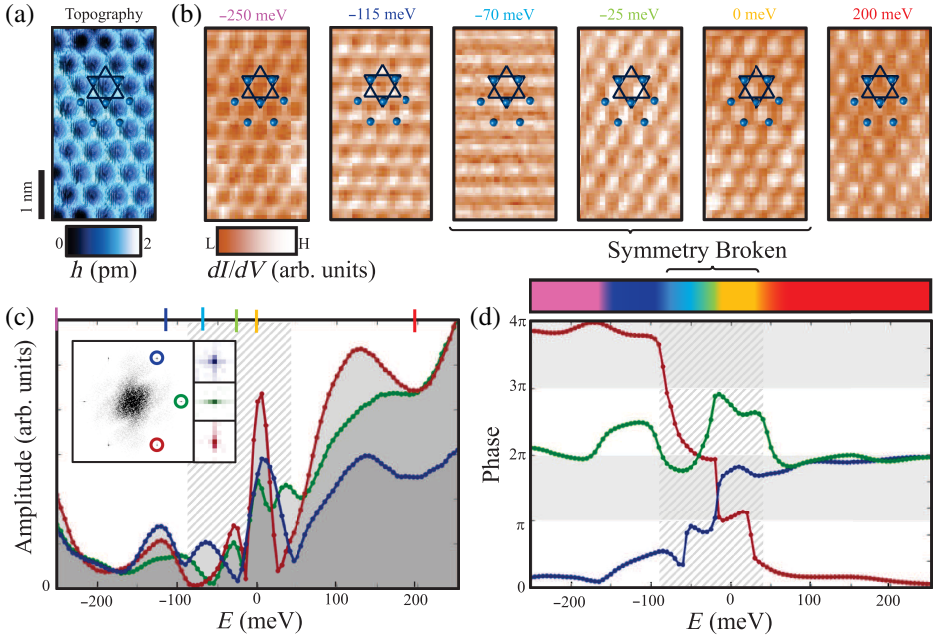

FIG. 2. Cascade of nematic phase shifts. (a) Topographic image of the Co_3Sn surface with a commensurate kagome lattice overlaid. (b) dI/dV maps of the same region in (a) at various energies with the kagome lattice overlaid at a fixed position. (c) The amplitudes of the three Bragg peaks of the FT dI/dV maps (see one shown explicitly in the inset with enlarged panels on the peaks). (d) Phase evolution of the same three Bragg peaks in energy.

attempt to position the kagome-coordinated Co atoms, we fail to do so in a way that will respect the symmetry of the periodic patterns across all energies imaged. We succeed in doing so consistently only away from the Fermi energy at high and low bias—below about −100 meV and above 50 meV. At all intermediate energies about the Fermi energy, we find atomic scale dI/dV distributions that seem to peak at locations that are not symmetry points of the underlying ionic kagome crystal, which remains fixed throughout the measurement.

Yet, the bare spatial resolution within a single unit cell provided by the spectroscopic raw mappings is marginal for firmly concluding that the electronic structure breaks the symmetry imposed by the ionic lattice. Nevertheless, the extended two-dimensional spatial mapping of hundreds of identical unit cells introduces redundancy, which we use to demonstrate nematicity beyond doubt. One method to exploit this is by a Fourier transformation (FT), which resolves the periodic patterns across the extended field of view. We clearly identify the three nonequivalent Bragg peaks corresponding to the unit cell period in the spatial spectroscopic mappings, circled in the inset of Fig. 2(c). The right-hand panels of the inset show enlarged images of the Bragg peaks and their corresponding colors. They consist of a single strong pixel surrounded by a faint crosslike halo that originates mainly from the finite window size, while drift seems negligible. The main panel shows the energy dependence of the amplitudes of the central pixels of the three Bragg peaks, colored accordingly. We find a series of approximate sharp nodes around zero bias at which the amplitude of some or all Bragg peaks almost vanishes. Between those nodes, the amplitudes of the Bragg peaks are strongly unbalanced, while beyond this interval, they are all finite and fairly equal. We note that, unlike the reproducibility of the nodes and phase shifts at intermediate energies, the slight anisotropy in the magnitude of the Bragg peaks at low and high energies seems to somewhat vary between different spectroscopic maps [36] and thus does not seem to signify nematicity.

Even more striking, though, is what we find in the phase information of the FT Bragg peaks, displayed in Fig. 2(d). Since the DOS we image is a real positive quantity, its FT is a complex number, $A_{\boldsymbol{q}}\exp(i\Phi_{\boldsymbol{q}})$. Its phase $\Phi_{\boldsymbol{q}}$ entails the phase shift $\boldsymbol{\delta}_{\boldsymbol{q}}$ with which the periodic pattern of corresponding wavelength $\boldsymbol{q}$ is positioned in real space, such that $\Phi_{\boldsymbol{q}} = \boldsymbol{q}\cdot\boldsymbol{\delta}_{\boldsymbol{q}}$. For the Bragg peaks that we inspect here, the $\boldsymbol{q}$ values are the three reciprocal wave vectors of the kagome crystal. Remarkably, we find at the vicinity of zero bias a sequence of three abrupt phase jumps by a fraction of 2π and thus correspond to real space shifts of the electronic wave function by a fraction of the unit cell vectors [36]. As the real-space direct mapping hints, at least some of the wave function distributions about the Fermi energy violate the symmetry imposed by the ionic lattice and are thus nematic. Between high and low energies, on the other hand, the phases of the Bragg peaks differ by approximately integer multiples of 2π, confirming that away from zero bias the wave function structure adheres to the underlying ionic lattice. Intriguingly, however, the phases at highest bias do not recover to their values at low bias, as will be discussed later. Every abrupt phase jump is accompanied by a node in the Bragg peak amplitude. We use the phase jumps and nodes to identify five energy intervals, indicated by the color bar in Fig. 2(d) and in later figures. We obtain the corresponding evolution of the real-space DOS distribution by inverse Fourier transforming the amplitude and phase information of the Bragg peaks [36]. Far from the Fermi energy we indeed recover DOS distributions that respect the underlying symmetries of the kagome lattice, while at the Fermi energy and slightly below it they seem to break the rotational symmetry of the lattice.

Yet, in order to directly obtain the exact wave function patterns and their changes with respect to the quenched ionic lattice, we aim to achieve superior resolution directly in real space. For this, we use the redundancy in mapping multiple equivalent unit cells to construct a superresolved single unit cell [48]. It relies on the incommensurability between the ionic lattice, which in the present case has a kagome structure, and the rectangular grid at which the STM measurement probes, as well as the inevitable mismatch in the exact lattice constants of the two. As a result, the unit cell is repeatedly probed at thousands of different points over the periodic unit cell structure, which can be collapsed into a single, superresolved unit cell [36].

The results of applying this procedure are presented in Fig. 3(a) [36]. It shows the wave function distribution across the superresolved unit cell at different energies of interest, each tiled six more times to make the spatial periodicity apparent. We indeed confirm with great clarity that the wave function distribution at low and high energies, below −150 meV and above 50 meV (Tri1− and Tri1+ panels, respectively), is the same. Above −150 meV and up to about −80 meV, the wave function shifts within the unit cell to a different position. To compare wave function distributions across different energy intervals, we extract equi-intensity contours at a value 10% below the maximum. Such wave function contours, representative of the three energy intervals discussed thus far, are overlaid in Fig. 3(b). The similar distribution at the highest and lowest energy intervals (red and magenta, respectively) is evident. The contours from the adjacent negative energy interval (blue contours) reside over subsurface S sites, complementing them to a kagome pattern. We thus use these unperturbed wave function distributions to position the underlying kagome lattice [balls and sticks in Fig. 3(a) and gray triangles in Figs. 3(b) and 3(c)] in agreement with the symmetry of the topographic image.

Remarkably, the remaining energy interval closest to the Fermi energy of the superresolved unit cells reveals three distinct wave function distributions that do not respect the

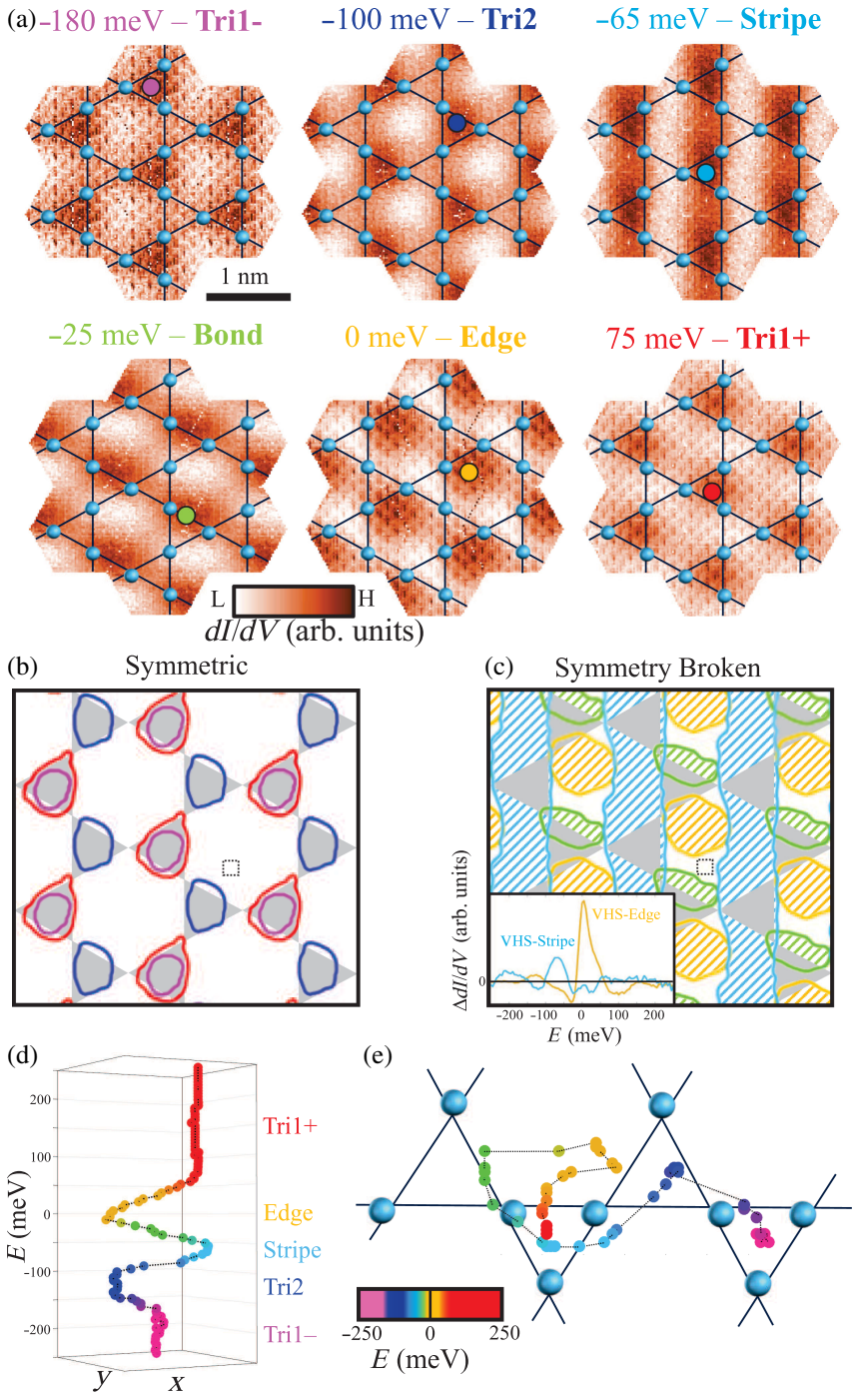

FIG. 3. Superresolution of spontaneous symmetry broken states. (a) Superresolved cells at the different energies with the kagome lattice overlaid on them. The circles mark the wave function's center of mass position. (b) [(c)] Contour maps of the wave functions from the superresolved cells at different energies away from [at the vicinity of] the Fermi energy in corresponding color. The inset of (c) shows the excess dI/dV spectrum localized within the positions of the nematic inner edge and stripe states (yellow and blue lines, respectively) relative to the extended background (averaged within the dotted square). (d) Energy evolution of the wave function's center of mass position. (e) Position path of the center of mass across all energies imaged showing a unit cell displacement is acquired.

determined ionic lattice symmetry, in accordance with the FT phase analysis [Fig. 2(d)]. Within the energy interval −80 to −35 meV, we find a stripelike wave function distribution. Picking one stripe orientation over the other two constitutes a spontaneous symmetry breaking of the C_3 rotation. We note that indeed within this energy interval the amplitude of a single Bragg peak dominates while the other two almost vanish, as shown in Fig. 2(c). About the Fermi

energy and within the interval of −20 to 50 meV, the wave function localizes at the inner edge of the central hexagon of the kagome pattern. Again, this location is equivalent to the two other edges related by C_3 symmetry and thus hallmarks spontaneous breaking of the C_3 symmetry of the original kagome lattice. In the narrow energy interval between −35 to −20 meV, the superresolved unit cell shows a distinct distribution which seems to be localized over a Co–Co bond and again breaks the C_3 symmetry. The narrow energy interval over which we observe the bond distribution may suggest it is an intermediate configuration between the edge and stripe states at higher and lower energy intervals.

The equidensity contour lines of the symmetry broken nematic states within the distorted kagome unit cell are displayed in Fig. 3(c). The location of the underlying kagome ions, fixed at high and low energies, is given by the gray triangles. The symmetry broken states seem to occupy different inner edges of the hexagonal region at different energy intervals. It also becomes clear that no position of the kagome ionic lattice will be commensurate with the wave function distributions across all energies. We rule out strain as the mechanism behind the symmetry broken wave function distributions because a distorted lattice results in distorted electronic states at all energies (as we demonstrate via *ab initio* calculations [36]) while the symmetry breaking we observe is limited to the vicinity of the Fermi energy. The superior intraunit cell resolution enables us also to extract the full energy spectrum of the excess DOS at specific points within it, where specific wave function distributions uniquely reside [Fig. 3(c) inset]. This further reveals that, while the zero-bias peak is localized on the yellow spots in Fig. 3(c), the striped distribution corresponds to a second peak in the DOS, with about half the density. This suggests that the nematic electronic distribution is accompanied by a splitting of a third of the DOS, which corresponds to the HOVHSs away from the Fermi energy.

This may still leave room for a response to feeble strain in case of strong nematic susceptibility, as seen for instance in FeSe compounds [49,50]. Since we do not detect any deviation of the Bragg peaks in high-resolution topographic images [36], we can put an upper bound for the amount of unit cell distortion, $\delta < 0.11\%$. On the other hand, the energy scale of the Fermi surface deformation we find, $E_{\mathrm{nem}} \approx 100$ meV, is rather large [51]. These would yield an enormous lower bound for the Co_3Sn nematic susceptibility, $\chi = E_{\mathrm{nem}}/\delta > 91$ eV, almost an order of magnitude larger than that found in FeSe [52]. However, we find no modification in the magnitude or directionality of the nematic states in the vicinity of adatoms and step edges [36], which surely modify the local strain field [53,54]. We thus conclude that the nematic wave function structures do not result from the conjunction of feeble strain and strong nematic susceptibility. We also learn from FeSe that, in bulk crystals, the nematic domains are very large in size, tens or even hundreds of microns [55,56]. It is only in thin films where nanometer-scale domains are formed [57,58], which may explain why we did not detect any domains within the spontaneously symmetry broken states in the Co_3Sn termination of bulk $Co_3Sn_2S_2$. We also rule out tip effects in inducing the nematic distributions, by mapping the spectroscopy across the Co_3Sn to S step edge [36], showing that the latter does not exhibit nematicity while the former does.

The superresolved cells enable us to closely follow the exact redistribution of the wave function with energy beyond the representative snapshots displayed in Fig. 3(a). For this, we calculate the "center of mass" of the wave function as a function of energy: $\mathbf{r}_{\mathrm{c.m.}} = \int_{\mathrm{uc}} d\mathbf{r}' |\Psi(E, \mathbf{r}')|^2 \mathbf{r}'$. For example, the center of mass locations calculated for the snapshots in Fig. 3(a) are given by the solid circles, while their full energy evolution is shown in Fig. 3(d). The distribution of the unoccupied states, as well as that of core energies, is completely quenched, showing no energy dependence. Only a thin shell of about 100 meV around the Fermi level of mainly occupied states shows rapid redistribution. The edge and stripe states (yellow and light blue, respectively) are stable over finite energy intervals. In contrast, the intermediate bond state (green) indeed seems more as a transient between them.

Following accurately the wave function center of mass progression across the distorted kagome unit cell, as shown in Fig. 3(e), reveals another remarkable property that is not apparent through the individual snapshots. We find that the high- and low-energy distributions, which at first glance appear identical, rather accumulate a relative shift of a full unit cell vector. This unit cell shift is in accord with the relative 2π phase offsets of the Bragg peaks between high and low energies we have observed in Fig. 2(d). Recently, it has been shown that the evolution of the charge center with bias voltage can be directly tied to band topology [59,60], but we leave a closer analysis of this question to future work. We speculate it may have an effect on boundaries at step edge terminations, where we have indeed previously reported the appearance of an edge accumulation at about −100 meV [61].

We thus identify two nematic electronic states, one at the Fermi energy and one about 60 meV below it, that spontaneously break rotational symmetry of the underlying lattice but do not break its translational symmetry. We attribute the appearance of the two nematic states to a d-wave Pomeranchuk instability. With the onset of Pomeranchuk order, the distorted kagome band structure further deforms such that saddle points at a subset of the M points are pushed down away from the Fermi energy, demonstrated in Fig. 4(a) by comparison of M_1 with M_2 and M_3, spontaneously breaking the threefold rotational symmetry of the distorted kagome lattice. To describe the interacting instabilities of this theory, we develop a patch

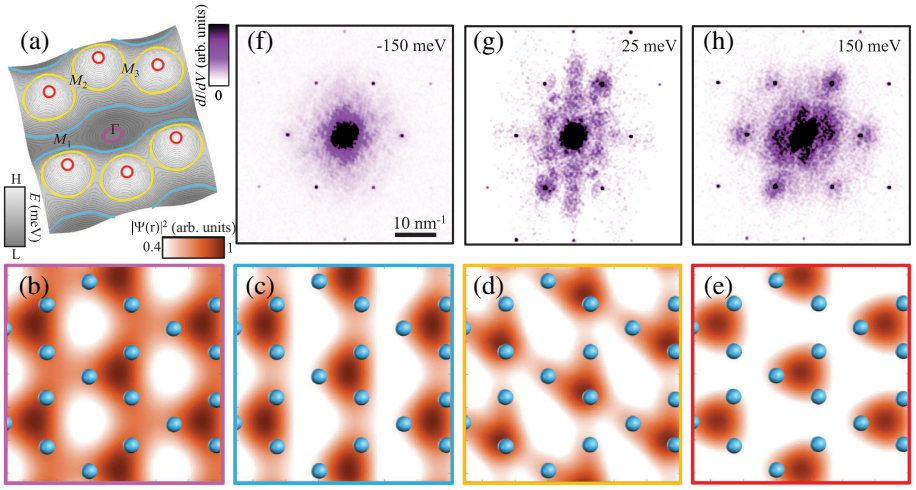

FIG. 4. *d*-wave Pomeranchuk instability to a nematic state. (a) Calculated kagome band structure of the tight-binding Hamiltonian perturbed by the *d*-wave Pomeranchuk order parameter. (b)–(e) Local DOS calculated using the perturbed tight-binding Hamiltonian, ranging from high to low energies [frame color corresponds to equienergy contours in (a)]. The lattice sites are denoted by blue spheres. At low and high energies, the DOS respects the lattice symmetry, while close to the Fermi energy we find nematic distributions (middle panels). (f)–(h) QPI showing C_3 symmetry broken pattern at the vicinity of the Fermi energy (g) and symmetric away from it (f) and (h).

model that incorporates the degrees of freedom located near the three M points where the DOS is largest [36]. The interacting model of an HOVHS is equivalent to a model developed previously [7], though the renormalization group equations themselves differ slightly due to the fact that $Co_3Sn_2S_2$ is a ferromagnet, and so there is no spin degeneracy in the present case. With the assumption that the largest interaction matrix elements are between states with small momentum transfer, *d*-wave Pomeranchuk order appears already at the mean-field level. We find, moreover, that *d*-wave Pomeranchuk order remains the leading instability of the model upon including corrections beyond mean field, introduced by integrating out the degrees of freedom away from the Fermi surface, which produces a renormalization group flow.

The resulting ground state is a linear combination of two *d*-wave form factors $\mathcal{O}_1(k_x^2 - k_y^2) + \mathcal{O}_2 2k_x k_y$. The fact that these states are translationally symmetric charge orders means the Landau free energy possesses a cubic term $\mathcal{F}_3 = \mathcal{O}_1^3 - 3\mathcal{O}_1\mathcal{O}_2^2$, resulting in a minimum of the free energy in which $O_{1,2}$ are nonzero at all three M points, but largest at one particular spontaneously chosen M point, producing a charge nematic state as shown in Fig. 4(a). Adding such a Pomeranchuk order parameter to the tight-binding model, we calculate the resulting local DOS at different energies [corresponding to equienergy contours in Fig. 4(a)] shown in Figs. 4(b)–4(e). At intermediate energies [Figs. 4(c) and 4(d)], we indeed recover a nematic wave function distribution following from the *d*-wave Pomeranchuk distortion of the Fermi surface. The wave function at lower energies resembles a stripe distribution, and the wave function at higher energies localizes at a point that breaks the rotational symmetry of the lattice. We stress that both these nematic distributions reflect the single Pomeranchuk distortion of the band structure by which a single pair of HOVHS shifts to lower energies by about 80 meV, while a double pair remains degenerate at zero bias. It is also consistent with the splitting of the two DOS peaks shown in the inset of Fig. 3(c). At high and low energies, the wave function distribution becomes symmetric, as observed experimentally [Figs. 4(b) and 4(e)]. While our accompanying theoretical investigation suggests a *d*-wave Pomeranchuk instability, further theory refinement will be necessary to rationalize all detailed features of the nematic phase we observe.

Finally, we carefully examine QPI patterns acquired over regions containing visible adatom impurities, which act as scatterers. As the scattered electrons interfere, they embed the wavelength of the transferred momentum $\mathbf{q}$ in the LDOS that can be resolved by FT. Such FT images are presented in Figs. 4(f)–4(h), close to and above the Fermi energy. Remarkably, close to the Fermi energy [Fig. 4(g)], we identify among the fairly symmetric QPI patterns an additional pattern dispersing radially along a single Γ–M direction. We attribute the absence of the C_3 symmetric counterparts to the removal of saddle points from the Fermi energy that eliminates those elastic scattering processes. Indeed, the deformed band structure under the Pomeranchuk instability hosts an elongated open pocket along the Γ–M_1 direction [Fig. 4(a)]. It is formed by the shift of a single pair of VHS relative to the other two. Such an open Fermi surface would host a similar scattering process. The QPI pattern goes symmetric away from the Fermi energy as demonstrated in Figs. 4(f) and 4(h) [36].

In summary, we have identified a mechanism by which distorted kagome lattices develop HOVHS at their *m*-type saddle point, realized on the Co_3Sn surface of

ferromagnetic $Co_3Sn_2S_2$, where the HOVHS is pinned at the Fermi energy. The manifestation of this effect is that the Fermi surface deforms, undergoing a Pomeranchuk instability by spontaneously displacing a subset of the three distinct saddle points to lower energies. As a result, the electronic states become nematic, and the wave functions break the symmetries of the underlying distorted kagome lattice, which we trace both in real space through the construction of superresolved unit cells and in reciprocal spaces through the phase and amplitude of the Bragg peaks. Our observations open the path for further explorations of HOVHS generation in other distorted kagome materials. Similar breathing kagome structures appear in the bulk of various materials. The M_3X family, as Mn_3Sn [20], Fe_3Sn [62], and Ni_3In [45], all host a breathing kagome structure, and so does $Ta_2V_{3.1}Si_{0.9}$ [63]. Moreover, various breathing distortions may result from charge density wave instabilities, which are common in kagome metals, as in CsV_3Sb_5 [24] that hosts a peculiar HOVHS near the Fermi level. It would be interesting to apply this mechanism to other flat band structural motifs, such as bipartite and pyrochlore lattices, wherein other forms of instabilities may be established.

ACKNOWLEDGMENTS

H. B. acknowledges funding by the Binational Science Foundation (NSF-BSF Materials: 2020744). R. T. was supported by the Deutsche Forschungsgemeinschaft (DFG, German Research Foundation) through Project No. 258499086—SFB 1170 and through the Wuerzburg-Dresden Cluster of Excellence on Complexity and Topology in Quantum Matter—ctd.qmat Project No. 390858490—EXC 2147. B. Y. acknowledges the financial support by the Israel Science Foundation (ISF: 2974/23). J. S. acknowledges support from the Paulo Pinheiro de Andrade fellowship. R. Q. and J. I. were supported by the NSF MRSEC program at Columbia through the Center for Precision-Assembled Quantum Materials (DMR-2011738).

DATA AVAILABILITY

The data that support the findings of this article are openly available.

[1] L. Van Hove, *The occurrence of singularities in the elastic frequency distribution of a crystal*, Phys. Rev. **89**, 1189 (1953).

[2] A. Shtyk, G. Goldstein, and C. Chamon, *Electrons at the monkey saddle: A multicritical Lifshitz point*, Phys. Rev. B **95**, 035137 (2017).

[3] N. F. Q. Yuan, H. Isobe, and L. Fu, *Magic of high-order van Hove singularity*, Nat. Commun. **10**, 5769 (2019).

[4] A. Chandrasekaran, A. Shtyk, J. J. Betouras, and C. Chamon, *Catastrophe theory classification of Fermi surface topological transitions in two dimensions*, Phys. Rev. Res. **2**, 013355 (2020).

[5] A. Chandrasekaran and J. J. Betouras, *A practical method to detect, analyze, and engineer higher order van Hove singularities in multi-band Hamiltonians*, Adv. Phys. Res. **2**, 2200061 (2023).

[6] A. Chandrasekaran *et al.*, *Engineering higher order van Hove singularities in two dimensions: The example of the surface layer of* Sr_2RuO_4, Nat. Commun. **15**, 9521 (2024).

[7] L. Classen, A. V. Chubukov, C. Honerkamp, and M. M. Scherer, *Competing orders at higher-order Van Hove points*, Phys. Rev. B **102**, 125141 (2020).

[8] X. Han, A. P. Schnyder, and X. Wu, *Enhanced nematicity emerging from higher-order Van Hove singularities*, Phys. Rev. B **107**, 184504 (2023).

[9] J. Beck, J. Bodky, M. Dürrnagel, R. Thomale, J. Ingham, L. Klebl, and H. Hohmann, *Kekulé order from diffuse nesting near higher-order Van Hove points*, Phys. Rev. Lett. **136**, 106503 (2026).

[10] X. Lu *et al.*, *Superconductors, orbital magnets and correlated states in magic-angle bilayer graphene*, Nature (London) **574**, 653 (2019).

[11] E. Y. Andrei and A. H. MacDonald, *Graphene bilayers with a twist*, Nat. Mater. **19**, 1265 (2020).

[12] A. Uri *et al.*, *Mapping the twist-angle disorder and Landau levels in magic-angle graphene*, Nature (London) **581**, 47 (2020).

[13] H. Zhou *et al.*, *Isospin magnetism and spin-polarized superconductivity in Bernal bilayer graphene*, Science **375**, 774 (2022).

[14] S. C. Barrera *et al.*, *Cascade of isospin phase transitions in Bernal-stacked bilayer graphene at zero magnetic field*, Nat. Phys. **18**, 771 (2022).

[15] A. M. Seiler *et al.*, *Quantum cascade of correlated phases in trigonally warped bilayer graphene*, Nature (London) **608**, 298 (2022).

[16] H. Zhou *et al.*, *Superconductivity in rhombohedral trilayer graphene*, Nature (London) **598**, 434 (2021).

[17] A. Guerrero-Avilés *et al.*, *Rhombohedral trilayer graphene is more stable than its Bernal counterpart*, Nanoscale **14**, 16295 (2022).

[18] J. X. Yin, B. Lian, and M. Z. Hasan, *Topological kagome magnets and superconductors*, Nature (London) **612**, 647 (2022).

[19] L. Ye *et al.*, *Hopping frustration-induced flat band and strange metallicity in a kagome metal*, Nat. Phys. **20**, 610 (2024).

[20] S. S. Zhang *et al.*, *Many-body resonance in a correlated topological kagome antiferromagnet*, Phys. Rev. Lett. **125**, 046401 (2020).

[21] C. Chen, J. Zheng, Y. He, S. Wu, X. Ying, S. Sankar, L. Li, Y. Wei, X. Dai, H. C. Po *et al.*, *Nematic order and orbital selective Mott state in a partially filled kagome flat band*, Phys. Rev. X **16**, 011009 (2026).

[22] T. Neupert, M. M. Denner, J. X. Yin, R. Thomale, and M. Z. Hasan, *Charge order and superconductivity in kagome materials*, Nat. Phys. **18**, 137 (2022).

[23] Y. Luo *et al.*, *A unique van Hove singularity in kagome superconductor* $CsV_{3-x}Ta_xSb_5$ *with enhanced superconductivity*, Nat. Commun. **14**, 3819 (2023).

[24] Y. Hu *et al.*, *Rich nature of van Hove singularities in kagome superconductor* CsV_3Sb_5, Nat. Commun. **13**, 2220 (2022).

[25] M. Kang *et al.*, *Twofold van Hove singularity and origin of charge order in topological kagome superconductor* CsV_3Sb_5, Nat. Phys. **18**, 301 (2022).

[26] H. D. Scammell, J. Ingham, T. Li, and O. P. Sushkov, *Chiral excitonic order from twofold van Hove singularities in kagome metals*, Nat. Commun. **14**, 605 (2023).

[27] J. Ingham, R. Thomale, and H. D. Scammell, *Vestigial order from an excitonic mother state in kagome superconductors* AV_3Sb_5, arXiv:2503.02929.

[28] L. Nie *et al.*, *Charge-density-wave-driven electronic nematicity in a kagome superconductor*, Nature (London) **604**, 59 (2022).

[29] X. Teng *et al.*, *Discovery of charge density wave in a kagome lattice antiferromagnet*, Nature (London) **609**, 490 (2022).

[30] J. X. Yin *et al.*, *Discovery of charge order and corresponding edge state in kagome magnet FeGe*, Phys. Rev. Lett. **129**, 166401 (2022).

[31] H. Li *et al.*, *Electronic nematicity without charge density waves in titanium-based kagome metal*, Nat. Phys. **19**, 1591 (2023).

[32] Y. X. Jiang *et al.*, *Van Hove annihilation and nematic instability on a kagome lattice*, Nat. Mater. **23**, 1214 (2024).

[33] N. Morali *et al.*, *Fermi-arc diversity on surface terminations of the magnetic Weyl semimetal* $Co_3Sn_2S_2$, Science **365**, 1286 (2019).

[34] D. F. Liu *et al.*, *Magnetic Weyl semimetal phase in a kagomé crystal*, Science **365**, 1282 (2019).

[35] J. X. Yin *et al.*, *Negative flat band magnetism in a spin–orbit-coupled correlated kagome magnet*, Nat. Phys. **15**, 443 (2019).

[36] See Supplemental Material at http://link.aps.org/supplemental/10.1103/2jst-psds for more information on surface identification (Sec. S2); Sec. S7 for more information on fitting of the zero-bias dI/dV; Sec. S8 for more information on QPI on the Sn termination; Sec. S3 for more information on the *ab initio* calculation; Sec. S4 for more information on fitting the *ab initio* HOVHS and its orbital character; Fig. S5 for more information on the dispersion of the *ab initio* HOVHS; Sec. S5 for more information on the orbital character of the HOVHS; Sec. S6 for more information on the theoretical model; Sec. S9 for more information on reproducibility of the nematic structure across dI/dV maps; Sec. S11 for more information on reproducibility of the Fourier analysis of the Bragg peaks; Sec. S10 for more information on inverse Fourier analysis of the Bragg peaks; Sec. S12 for more information on construction of the superresolved unit cell; Sec. S13 for more information on the full energy evolution of the superresolved wave function structure; Sec. S14 for more information on strain analysis; Sec. S15 for more information on ruling out tip effects; Sec. S16 for more information on QPI imaging of nematicity; which included Refs. [37–40].

[37] G. Kresse and J. Furthmüller, *Efficient iterative schemes for ab initio total-energy calculations using a plane-wave basis set*, Phys. Rev. B **54**, 11169 (1996).

[38] J. P. Perdew, K. Burke, and M. Ernzerhof, *Generalized gradient approximation made simple*, Phys. Rev. Lett. **77**, 3865 (1996).

[39] S. Grimme, J. Antony, S. Ehrlich, and H. Krieg, *A consistent and accurate ab initio parametrization of density functional dispersion correction (DFT-D) for the 94 elements H-Pu*, J. Chem. Phys. **132**, 154104 (2010).

[40] M. J. Lawler *et al.*, *Intra-unit-cell electronic nematicity of the high-*T_c *copper-oxide pseudogap states*, Nature (London) **466**, 347 (2010).

[41] Y. Xing, J. Shen, H. Chen, L. Huang, Y. Gao, Q. Zheng, Y.-Y. Zhang, G. Li, B. Hu, G. Qian *et al.*, *Localized spin-orbit polaron in magnetic Weyl semimetal* $Co_3Sn_2S_2$, Nat. Commun. **11**, 5613 (2020).

[42] L. Huang, X. Kong, Q. Zheng, Y. Xing, H. Chen, Y. Li, Z. Hu, S. Zhu, J. Qiao, Y.-Y. Zhang *et al.*, *Discovery and construction of surface kagome electronic states induced by p-d electronic hybridization in* $Co_3Sn_2S_2$, Nat. Commun. **14**, 5230 (2023).

[43] Z. Guguchia, J. Verezhak, D. Gawryluk, S. Tsirkin, J.-X. Yin, I. Belopolski, H. Zhou, G. Simutis, S.-S. Zhang, T. Cochran *et al.*, *Tunable anomalous Hall conductivity through volume-wise magnetic competition in a topological kagome magnet*, Nat. Commun. **11**, 559 (2020).

[44] Q. Li, H. Zhang, Y. Wang, W. Chen, C. Bao, Q. Liu, T. Lin, S. Zhang, H. Zhang, K. Watanabe *et al.*, *Evolution of the flat band and the role of lattice relaxations in twisted bilayer graphene*, Nat. Mater. **23**, 1070 (2024).

[45] J. C. Souza, M. Haim, A. Gupta, M. Mahankali, F. Xie, Y. Fang, L. Chen, S. Fang, H. Tan, M. Han *et al.*, *Origin of strange metallicity in a d-orbital kagome metal*, Nat. Phys. **22**, 541 (2026).

[46] J. Xiao, A. Inbar, J. Birkbeck, N. Gershon, Y. Zamir, T. Taniguchi, K. Watanabe, E. Berg, and S. Ilani, *Imaging the flat bands of magic-angle graphene reshaped by interactions*, Nature (London) **653**, 68 (2026).

[47] D. Di Sante, B. Kim, W. Hanke, T. Wehling, C. Franchini, R. Thomale, and G. Sangiovanni, *Electronic correlations and universal long-range scaling in kagome metals*, Phys. Rev. Res. **5**, L012008 (2023).

[48] I. Zeljkovic, E. J. Main, T. L. Williams, M. Boyer, K. Chatterjee, W. Wise, Y. Yin, M. Zech, A. Pivonka, T. Kondo *et al.*, *Scanning tunnelling microscopy imaging of symmetry-breaking structural distortion in the bismuth-based cuprate superconductors*, Nat. Mater. **11**, 585 (2012).

[49] R. Fernandes, A. Chubukov, and J. Schmalian, *What drives nematic order in iron-based superconductors?*, Nat. Phys. **10**, 97 (2014).

[50] A. E. Böhmer, J.-H. Chu, S. Lederer, and M. Yi, *Nematicity and nematic fluctuations in iron-based superconductors*, Nat. Phys. **18**, 1412 (2022).

[51] M. Yi, H. Pfau, Y. Zhang, Y. He, H. Wu, T. Chen, Z. Ye, M. Hashimoto, R. Yu, Q. Si *et al.*, *Nematic energy scale and the missing electron pocket in FeSe*, Phys. Rev. X **9**, 041049 (2019).

[52] H. Pfau, S. Chen, M. Yi, M. Hashimoto, C. Rotundu, J. Palmstrom, T. Chen, P.-C. Dai, J. Straquadine, A. Hristov

et al., *Momentum dependence of the nematic order parameter in iron-based superconductors*, Phys. Rev. Lett. **123**, 066402 (2019).

[53] G. Leibfried and N. Breuer, *Point Defects in Metals I: Introduction to the Theory* (Springer, New York, 2006).

[54] W. Li, H. Duan, K. Albe, and J. Weissmüller, *Line stress of step edges at crystal surfaces*, Surf. Sci. **605**, 947 (2011).

[55] T. Shimojima, Y. Motoyui, T. Taniuchi, C. Bareille, S. Onari, H. Kontani, M. Nakajima, S. Kasahara, T. Shibauchi, Y. Matsuda *et al.*, *Discovery of mesoscopic nematicity wave in iron-based superconductors*, Science **373**, 1122 (2021).

[56] T. Hashimoto, Y. Ota, H. Q. Yamamoto, Y. Suzuki, T. Shimojima, S. Watanabe, C. Chen, S. Kasahara, Y. Matsuda, T. Shibauchi *et al.*, *Superconducting gap anisotropy sensitive to nematic domains in FeSe*, Nat. Commun. **9**, 282 (2018).

[57] Y. Yuan, W. Li, B. Liu, P. Deng, Z. Xu, X. Chen, C. Song, L. Wang, K. He, G. Xu *et al.*, *Edge states at nematic domain walls in FeSe films*, Nano Lett. **18**, 7176 (2018).

[58] Z. Ren, H. Li, H. Zhao, S. Sharma, Z. Wang, and I. Zeljkovic, *Nanoscale decoupling of electronic nematicity and structural anisotropy in FeSe thin films*, Nat. Commun. **12**, 10 (2021).

[59] M. Holbrook, J. Ingham, D. Kaplan, L. N. Holtzman, B. Bierman, B. Hou, N. Olsen, L. Nashabeh, Y. Li, S. Liu, X. Zhu, D. Y. Qiu, D. Rhodes, K. Barmak, J. C. Hone, R. Queiroz, and A. N. Pasupathy, *Real-space imaging of the band topology of transition metal dichalcogenides*, Nat. Phys. **22**, 680 (2026).

[60] J. Ingham and R. Queiroz, *Real-space imaging of band topology via wavefunction zeros*, arXiv:2503.02929.

[61] S. Howard *et al.*, *Evidence for one-dimensional chiral edge states in a magnetic Weyl semimetal* $Co_3Sn_2S_2$, Nat. Commun. **12**, 4269 (2021).

[62] J.-X. Yin, S. S. Zhang, H. Li, K. Jiang, G. Chang, B. Zhang, B. Lian, C. Xiang, I. Belopolski, H. Zheng *et al.*, *Giant and anisotropic many-body spin-orbit tunability in a strongly correlated kagome magnet*, Nature (London) **562**, 91 (2018).

[63] H. Liu, J. Yao, J. Shi, Z. Yang, D. Yan, Y. Li, D. Chen, H. L. Feng, S. Li, Z. Wang *et al.*, *Vanadium-based superconductivity in the breathing kagome compound* $Ta_2V_{3.1}Si_{0.9}$, Phys. Rev. B **108**, 104504 (2023).